ISSN (Print) 1226-1750
ISSN (Online) 2233-6656
Journal of Magnetics 31(3), 385-390 (2026) https://doi.org/10.4283/JMAG.2026.31.3.385

The Static and Dynamic Properties of Chemically Synthesized Cubic-shaped Superparamagnetic Iron Oxide Nanoparticles

Misun Kang[1†], Jaehun Cho[2,3†], Da Hyun Lee[3], Sung Jun Lim[2,3]*, and Jae Young Bae[1]*

[1]*Department of Chemistry, Keimyung University, Daegu 42601, Republic of Korea*
[2]*Industrial AX Innovation Research Institute, AX Research Group for Semiconductor, Daegu Gyeongbuk Institute of Science and Technology (DGIST), Daegu 42988, Republic of Korea*
[3]*Division of Nanotechnology, Daegu Gyeongbuk Institute of Science and Technology (DGIST), Daegu 42988, Republic of Korea*

(Received 24 July 2026, Received in final form 6 August 2026, Accepted 6 August 2026)

Cubic and spherical superparamagnetic iron oxide nanoparticles with comparable diameters are chemically synthesized via thermal decomposition to investigate shape-dependent characteristics. Various measurements reveal that nanocubes exhibit higher saturation magnetization, larger coercivity, and elevated blocking temperature relative to nanospheres due to the reduced surface spin disorder and stronger shape anisotropy. Electron spin resonance spectroscopy exhibits a resonance field shift and linewidth broadening in cubic particles based on the enhanced effective anisotropy. Micromagnetic simulations support these trends that cube edge-length variation induces resonance splitting absent in spheres, supporting cubic superparamagnetic iron oxide nanoparticles as promising candidates for hyperthermia and imaging agent applications.

Keywords : Fe_3O_4 nano particles, superparamagnetism, electron spin resonance, micromagnetics

1. Introduction

Superparamagnetic iron oxide nanoparticles (SPIONs), among the smallest multi-functional magnetic nanomaterials, have attracted significant attention in biomedical fields due to their unique magnetic properties and excellent biocompatibility [1, 2]. Unlike bulk ferromagnetic materials, SPIONs exhibit zero remanent magnetization and coercivity, becoming magnetized only under an external field and losing magnetism once it is removed [3, 4]. This superparamagnetic behavior enables precise, remote control without inducing unwanted aggregation in vivo, while surface functionalization with biocompatible polymers and ligands allows targeted interaction with biological molecules for selective diagnostic and therapeutic applications [5-7].

Biomedical use of SPIONs requires both high saturation magnetization (M_s) for effective magnetic responsiveness and negligible remanence/coercivity to prevent aggregation and ensure reversibility [8]. However, increasing M_s via larger particle size often induces ferromagnetism, characterized by hysteresis and residual magnetization—reducing colloidal stability and promoting undesirable aggregation.

Superparamagnetism is a magnetic phenomenon observed in single-domain nanoparticles, typically below 50 nm, where thermal energy (k_BT) is sufficient to overcome the magnetic anisotropy energy barrier ($K_{eff}V$). This causes the magnetic moments of individual particles to randomly flip their direction, leading to a zero net magnetization in the absence of an external magnetic field. The characteristic time scale for these flips is defined by the Néel relaxation time (τ_N), which is exponentially dependent on the particle's volume (V), magnetic anisotropy constant (K_{eff}), and temperature (T), as described by the Néel-Arrhenius equation:

$$\tau_N = \tau_0 e^{\frac{K_{eff}V}{k_BT}}. \quad (1)$$

A critical point in this behavior is the blocking temperature (T_B), the temperature below which the nanoparticles' magnetic moments become "blocked" in a specific orientation, exhibiting a behavior similar to ferromagnetism. The

©The Korean Magnetics Society. All rights reserved.
*Co-corresponding author: Tel: +82-53-785-3502
E-mail: melsj@dgist.ac.kr (Sung Jun Lim)
Tel: +82-53-580-5186, E-mail: jybae@kmu.ac.kr (Jae Young Bae)
†These authors contributed equally to this work.

© 2026 Journal of Magnetics

blocking temperature is not a fixed material property but is determined by the balance between the Néel relaxation time and the measurement time (τ_M), following the relationship:

$$T_B = \frac{KV}{k_B \ln\left(\frac{\tau_M}{\tau_0}\right)}. \quad (2)$$

Traditionally, research on iron oxide magnetic nanoparticles has focused on spherical geometries. However, recent efforts have increasingly targeted anisotropic morphologies, including nanocubes, nanorods, nanoflowers, and octapods, since shape control can significantly enhance both magnetic behaviors and biological activities. By leveraging shape anisotropy, researchers aim to overcome the traditional trade-off between saturation magnetization and superparamagnetic stability, marking a shift from simple synthesis toward deliberate, design-based nanostructure engineering.

In this study, we systematically investigate the static and dynamic magnetic properties of cubic-shaped SPIONs with an edge length of 10 to 12 nm, synthesized chemically and compared against similarly prepared spherical SPIONs. Static magnetic moments are characterized at room and low temperatures via Superconducting Quantum Interference Device - Vibrating Sample Magnetometer (SQUID-VSM) [9], while Electron Spin Resonance (ESR) is used to probe dynamic responses. As expected, cubic SPIONs exhibit a broader magnetic field response than spherical ones, attributed to shape anisotropy. Micromagnetic simulations of spin alignment and relaxation dynamics are performed for both morphologies, showing good agreement with experimental results.

2. Experiments

Iron oxide nanoparticles are synthesized via a high-temperature thermal decomposition method using a preformed Fe-oleate ($Fe(OL)_3$) precursor in 1-octadecene (ODE) in the presence of sodium oleate (NaOL). The Fe-oleate complex is first prepared by reacting ferric chloride hexahydrate ($FeCl_3 \cdot 6H_2O$, 40 mmol) with sodium oleate (120 mmol) in a mixed solvent of ethanol, distilled water, and hexane. The reaction mixture is heated to 70°C and maintained at that temperature for 4 h. The upper brown organic phase containing $Fe(OL)_3$ is then collected and purified by washing three times with distilled water, after which the mixture is evaporated to remove hexane, yielding a waxy solid iron-oleate complex. For the synthesis of spherical nanoparticles, a solution containing $Fe(OL)_3$ (5 mmol) and oleic acid (2.5 mmol) in 30 mL of ODE is loaded into a three-neck round-bottom flask and degassed under vacuum at 120°C for 60 min to remove residual moisture and oxygen. The atmosphere is then switched to Ar, and the mixture is heated to 318°C at a constant rate of 3.0°C min^{-1} and held at that temperature for 60 min. After cooling to room temperature, ethanol is added to induce precipitation, and the resulting spherical nanoparticles are isolated by centrifugation. For the synthesis of cubic nanoparticles, a solution containing $Fe(OL)_3$ (5 mmol) and NaOL (5 mmol) in 35 mL of ODE is similarly degassed under vacuum at 120°C for 60 min. The atmosphere is replaced with Ar, and the mixture is heated to 318°C at the same rate of 3.0°C min^{-1} and maintained for 60 min to enable cubic particle growth. After cooling to ambient temperature, ethanol is added to promote precipitation, and the cubic nanoparticles are recovered by centrifugation [10-12].

3. Results and Discussion

Transmission electron microscopy (TEM) images of the synthesized iron oxide nanoparticles are presented in Fig. 1. The spherical nanoparticles exhibit an average diameter of 10.51 ± 0.68 nm (see Fig. 1(a)), whereas the cubic nanoparticles display an average edge length of 11.35 ±

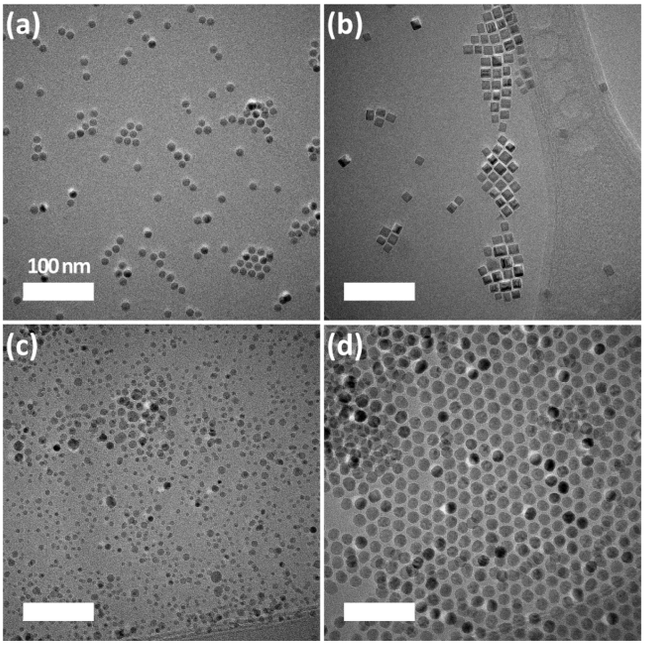


Fig. 1. Transmission electron microscopy (TEM) images of iron oxide nanoparticles. (a) Spherical nanoparticles with an average diameter of 10.51 ± 0.68 nm. (b) Cubic nanoparticles with an average edge length of 11.35 ± 1.00 nm. (c) Commercial iron oxide nanoparticles with a nominal diameter of 10 nm (Sigma-Aldrich). (d) Commercial iron oxide nanoparticles with a nominal diameter of 20 nm (Sigma-Aldrich). All scale bars represent 100 nm.

1.00 nm (see Fig. 1(b)). For comparison, commercially available cubic and spherical nanoparticles with nominal diameters of 10 nm and 20 nm are shown in Fig. 1(c) and Fig. 1(d), respectively. Both the spherical and cubic particles synthesized in this study demonstrate high mono-dispersity and uniform morphology, in contrast to the broader size distribution observed in the commercial 10 nm spherical sample. These results confirm that the employed thermal decomposition method enables precise control over nanoparticle shape and size, particularly near 10 nm, which is crucial for investigating shape-dependent magnetic properties [13, 14].

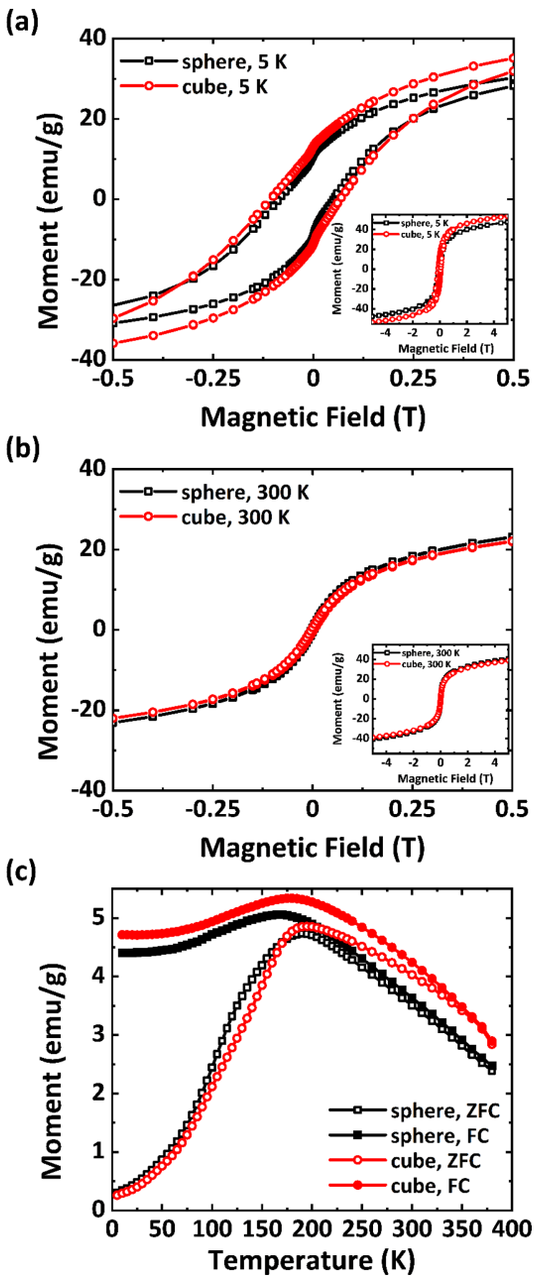


Fig. 2. (Color online) Static magnetic properties of spherical and cubic iron oxide nanoparticles measured by SQUID-VSM. (a, b) Field-dependent magnetization M(H) at 5 K and 300 K in near low applied field, respectively. The insets show full range of the M(H) curves. (c) ZFC and FC magnetization curves, indicating a blocking temperature (T_B) of around 190 K and 195 K for the spherical nanoparticles and the cubic nanoparticles, respectively.

For the static magnetic properties, the field-dependent magnetization, M(H), of the laboratory-synthesized Fe_3O_4 spherical and cubic nanoparticles is systematically examined by SQUID-VSM at 300 K and 5 K, as shown in Fig. 2(a) and (b). During the measurement, the nanoparticle samples are prepared in a powder form, where individual nanoparticles are randomly oriented with respect to the applied magnetic field, yielding a powder-averaged macroscopic magnetic response. At 300 K, both morphologies exhibit superparamagnetic behavior with negligible coercivity and remanence, and the M_s values are comparable, measured at 40.6 emu/g for the spherical nanoparticles and 38.9 emu/g for the cubic ones. At 5 K, the magnetic response transitions to a blocked ferromagnetic state, accompanied by a significant increase in M_s and the appearance of open hysteresis loops, with the cubic nanoparticles exhibiting a higher M_s of 53.5 emu/g compared to 47.6 emu/g for the spherical counterparts. This enhancement in low-temperature magnetization for the nanocubes is attributed to the suppressed surface spin disorder on the flat facets of the cubic morphology, whereas the higher curvature of the spheres likely induces a thicker magnetically dead layer [15, 16]. A distinct difference is also observed in the magnetic hardness, as quantified in Fig. 2(b), where the cubic nanoparticles display a noticeably larger coercivity field (H_c) of 86.7 mT compared to 69.0 mT for the spheres. This increased coercivity serves as direct experimental evidence of shape-induced anisotropy, which adds to the magnetocrystalline anisotropy and creates a higher energy barrier for magnetization reversal.

Fig. 2(c) presents the temperature-dependent magnetization, M(T), curves measured under zero-field cooling (ZFC) and field cooling (FC) protocols with an applied field of 10 mT, where the ZFC curves show a broad maximum corresponding to T_B. The T_B for the spherical nanoparticles is determined to be 190 K, while the cubic nanoparticles show a shift to a higher temperature of 195 K. Since the particle volumes, V are comparable, the relation $T_B \propto K_{eff}V \propto$ implies that the K_{eff} of the nanocubes is superior to that of the nanospheres, and the broadening of the ZFC peak in the cubic sample further suggests a wider distribution of energy barriers, likely arising from intensified dipolar interactions between the flat-faced particles.

The dynamic responses of the nanoparticles are probed

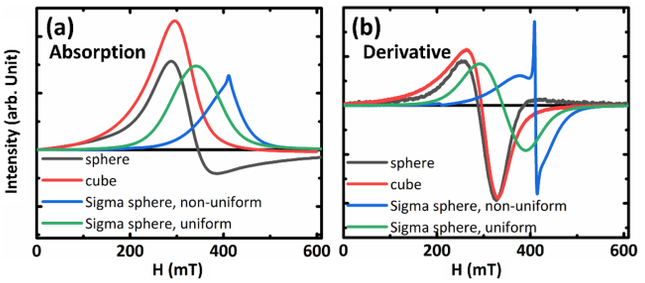


Fig. 3. (Color online) Dynamic magnetic properties of iron oxide nanoparticles obtained by electron spin resonance (ESR) at 9.16 GHz (*X*-band). (a) Absorption spectra and (b) Derivative spectra. Commercial non-uniform samples exhibited multi-peak features due to broad size distribution, while uniform spherical nanoparticles displayed narrower FWHM. Cubic nanoparticles showed a distinct resonance-field shift, reflecting the contribution of shape-induced magnetic anisotropy.

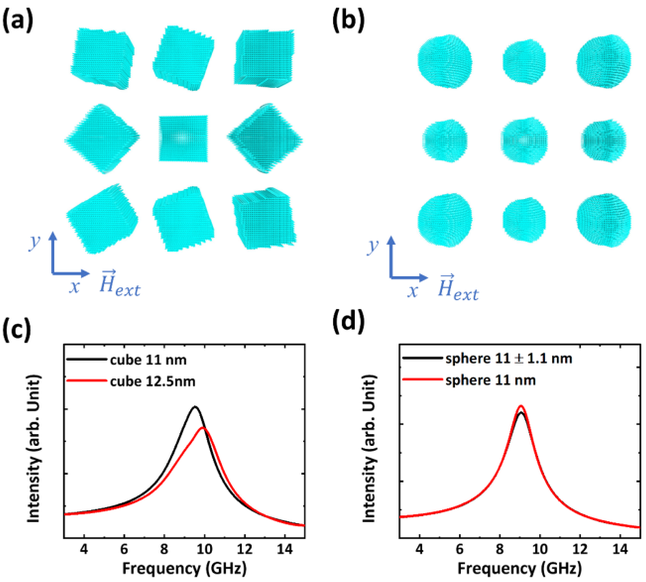


Fig. 4. (Color online) (a, b) Top-view configurations of cubes and spheres under external magnetic field (H_{ext}), where the cube assemblies were rotated by 10° increments around the *z*-axis to mimic powder averaging. (c) Simulated ferromagnetic resonance (FMR) spectra of cubes with edge lengths of 11 and 12.5 nm, showing multiple peak splitting and linewidth broadening with increasing size. (d) FMR spectra of spheres with identical size (11 nm) and ±10% radius variation, exhibiting negligible change in resonance behavior.

using ESR spectroscopy at 9.16 GHz (*X*-band) at room temperature to investigate the effect of particle shape and uniformity on magnetization dynamics, as shown in Fig. 3 [17]. Figs. 3(a) and (b) show the ESR spectra in absorption and derivative spectra, respectively. While the absorption curve indicates the actual magnitude of microwave absorption, the derivative form depicts the differentiation of this profile as a function of the magnetic field. Quantitatively, the resonance field extracted from the derivative spectra (Fig. 3(b)) shifts from approximately 285 mT for the spherical particles to approximately 294 mT for the cubic particles. This shift in resonance field reflects both the size of the SPIONs and the additional internal demagnetizing field imposed by the flat facets and sharp edges of the cubic geometry, relative to the uniform demagnetizing factor of a sphere. Furthermore, this shift is accompanied by linewidth broadening evidenced by an increase in the full width at half maximum (FWHM) from 96 mT for the spheres to 112 mT for the cubes. Even in a randomly oriented ensemble, the shape anisotropy of cubic geometry does not average out into an isotropic response. Instead, the distinct local anisotropy fields generated by the non-equivalent geometric dimensions such as the flat faces (a), face diagonals (√2 a), and corners (√3 a) induce significant inhomogeneous broadening across different orientations. By comparison, the resonance fields of commercial reference samples appear at markedly higher fields (337 mT for the uniform and 410 mT for the non-uniform commercial sphere) with larger or split linewidths, indicating a larger mean size and greater polydispersity than the in-house synthesized particles.

Consequently, commercial non-uniform samples display multiple peaks in the derivative spectra due to their broad size distribution, whereas the synthesized spherical nanoparticles exhibit a narrow, symmetric resonance with reduced full-width at half-maximum (FWHM), consistent with their uniform size distribution. However, cubic nanoparticles display a resonance-field shift compared with the spherical ones (See Fig. 3(a) and (b)). This shift originates from the contribution of shape anisotropy, which alters the internal demagnetizing field and thus modifies the resonance condition. The broader resonance features observed in the cubic nanoparticles highlight their sensitivity to morphological effects and suggest an enhanced capacity for radio frequency (RF) absorption across a wider field range, a behavior that is highly advantageous for biomedical applications such as magnetic resonance imaging and hyperthermia therapy.

To gain further insight into the experimental observations, micromagnetic simulations (Mumax3) are carried out for cubic and spherical nanoparticles (Fig. 4) [18-21]. The three-dimensional simulation geometries are depicted in Fig. 4(a) and (b). The material parameters in our simulations are summarized in Table 1. The simulations are performed by varying the single particle size to account for the different effective dimensions expected in a randomly oriented ensemble. The M_s is determined by SQUID-VSM results.

Table 1. Material parameters for micromagnetic simulations.

	Cubes	Spheres
Dimension (nm^3)	60 × 60 × 14	
Single particle dimension (nm^3)	(i) 11 × 11 × 11 (ii) 12.5 × 12.5 × 12.5	(i) Diameter = 11 (ii) Diameter = 11 ± 1.1
z- axis rotation	Every 10°	-
Repetition in (x, y, z)	(10, 10, 0)	
Unit cell (nm^3)	0.5 × 0.5 × 0.5	
M_s (kA/m)	480	
A_{ex} (pJ/m)	0.5	
α	0.07	
H_{ext} (mT)	(300, 0, 0)	
H_{rf} (mT)	(0, 0.5, 0)	
f_H (GHz)	50	
Total simulation time (ns)	100	

A_{ex} is set to be a small value to confine magnetic interaction within individual particles. Furthermore, magnetocrystalline anisotropy and the Dzyaloshinskii-Moriya interaction energy density are neglected. Under these conditions, the effective anisotropy, K_{eff} is primarily governed by the demagnetization energy determined by the particle geometry. Finally, the magnetic parameters for the background are set to zero. To ensure that the modeling is conducted under conditions equivalent to the ESR experiments, nine cubes and nine spheres with randomly distributed sizes and dimensions are defined as a single system following the TEM results in Fig. 1. For cubic assemblies, rotational averaging around the +z-axis in 10° increments is performed to reproduce powder-like experimental conditions. The RF magnetic field applied along the +y-axis is efficiently delivered to the system via a SINC function of the form $H(x, y, z) = H_{rf} \sin[2\pi f_H(t - t_0)]/2\pi f_H(t - t_0)$, thereby achieving broadband excitation suitable for probing ferromagnetic resonance (FMR) [22]. The simulation is carried out under the static magnetic field of 300 mT and rf magnetic field for 100 ns by taking t_0 = 50 ns in the above equation. The time step is taken to be 1 fs.

The simulated FMR spectra (Fig. 4(c) and (d)) clearly distinguish the two morphologies. In nanocubes, increasing the edge length from 11 to 12.5 nm results in resonance peak splitting and linewidth broadening, reflecting enhanced shape anisotropy effects. Conversely, spherical nanoparticles show nearly identical resonance profiles regardless of ±10% size variation, demonstrating their isotropic nature [23]. These results are in excellent agreement with the ESR measurements and confirm that cubic nanoparticles possess pronounced shape-induced anisotropy, leading to broader resonance profiles. Such linewidth broadening is expected to improve magnetic hyperthermia efficiency by enhancing RF energy coupling across a wider frequency range. Therefore, cubic nanoparticles represent a promising geometry for biomedical applications requiring efficient magnetic energy absorption and dissipation.

4. Summary

In summary, the combination of experimental data and micromagnetic modeling confirms that cubic SPIONs exhibit superior magnetic responses compared to spherical counterparts, largely due to shape anisotropy. These insights pave the way for rational nanostructure design, where particle morphology can be deliberately engineered to achieve optimal performance in specific biomedical and technological applications.

Acknowledgments

This research was supported by the Technology Innovation Program (RS-2024-00431493, Development of EV tires with 20% improvement in wear performance based on eco-friendly nano-composite) funded by the Ministry of Trade Industry & Energy (MOTIE, Korea). This work is also supported by the DGIST research programs (26-ET-02 and 26-SR-01).

References

[1] M. Mahmoudi, S. Sant, B. Wang, S. Laurent, and T. Sen, Adv. Drug Deliv. Rev. **63**, 24 (2011).
[2] J. Schemberg, A. El Abbassi, A. Lindenbauer, L.-Y. Chen, A. Grodrian, X. Nakos, G. Apte, N. Khan, A. Kraupner, T.-H. Nguyen, and G. Gastrock, ACS Appl. Mater. Interfaces **14**, 48011 (2022).
[3] B. Issa, I. M. Obaidat, B. A. Albiss, and Y. Haik, Int. J. Mol. Sci. **14**, 21266 (2013).
[4] O. Oehlsen, S. I. Cervantes-Ramírez, P. Cervantes-Avilés, and I. A. Medina-Velo, ACS Omega **7**, 3134 (2022).
[5] N. Sezer, İ. Arı, Y. Biçer, and M. Koç, J. Magn. Magn. Mater. **538**, 168300 (2021).
[6] H. Wang, Y. Hou, L. Chen, W. Mo, L. Xuan, J. Wu, J. Wang, M. Xie, S. Wang, and G. Tang, Biomed. Technol. **10**, 100084 (2025).
[7] A. M. A. Alobaidi and V. V. Kumeiko, Cancers **18**, 419 (2026).
[8] W. Yuan, M. Rojas-Ruiz, X. Sun, C. Shang, C. Giordano, and G. Zhang, Nanotechnology **37**, 262002 (2026).
[9] K. Lee, J. Cho, C.-K. Lee, J. Kim, C.-Y. You, M. Byun, and J.-S. Kim, J. Magn. Magn. Mater. **512**, 167057 (2020).
[10] J. Park, K. An, Y. Hwang, J.-G. Park, H.-J. Noh, J.-Y. Kim, J.-H. Park, and T. Hyeon, Nat. Mater. **3**, 891 (2004).

[11] J. Park, E. Lee, N.-M. Hwang, M. Kang, S. C. Kim, Y. Hwang, J.-G. Park, H.-J. Noh, J.-Y. Kim, J.-H. Park, and T. Hyeon, Angew. Chemie. Int. Ed. **44**, 2872 (2005).
[12] J. Park, J. Joo, S. Kwon, Y. Jang, and T. Hyeon, Angew. Chem. Int. Ed. **46**, 4630 (2007).
[13] V. Sandoval-Flores, J. A. Ortega-Cardenas, E. Ramon-Gallegos, G. F. Gutiérrez-López, D. Ravelo-Acuña, H. Yee-Madeira, and R. Mora-Escobedo, Mater. Res. Express **12**, 055401 (2025).
[14] B. T Simões, C. Chaparro, T. Vieira, M. A. Valente, M. C. V. Cavaco, V. Neves, J. C. Silva, J. P. Borges, F. V. Almeida, and P. Soares, Nano Express **6**, 015017 (2025).
[15] E. Wetterskog, C.-W. Tai, J. Grins, L. Bergström, and G. Salazar-Alvarez, ACS Nano **7**, 7132 (2013).
[16] A. Mitra, J. Mohapatra, and M. Aslam, Mater. Res. Express **11**, 022002 (2024).
[17] Y.-H. Choi, T. Yi, J. S. Park, and D.-K. Kim, J. Korean Ceram. Soc. **48**, 577 (2011).
[18] D. Aurélio and J. Vejpravova, Nanomaterials **10**, 1149 (2020).
[19] K. Brzuszek, C. A. Ross, and A. Janutka, J. Magn. Magn. Mater. **573**, 170651 (2023).
[20] A. Vansteenkiste, J. Leliaert, M. Dvornik, M. Helsen, F. García-Sánchez, and B. V. Waeyenberge, AIP Adv. **4**, 107133 (2014).
[21] C.-Y. You, J. Magn. **31**, 204 (2026).
[22] J. Cho, S. Miwa, K. Yakushiji, S. Tamaru, H. Kubota, A. Fukushima, S. Fujimoto, E. Tamura, C.-Y. You, S. Yuasa, and Y. Suzuki, Phys. Rev. B **94**, 184411 (2016).
[23] L. F. Gamarra, W. M. Pontuschka, J. B. Mamani, D. R. Cornejo, T. R. Oliveira, E. D. Vieira, A. J. Costa-Filho, and E. Amaro Jr., J. Phys.: Condens. Matter **21**, 115104 (2009).